AFRL-ML-WP-TR-1998-4184

INGAP/GAAS QUANTUM WELL INFRARED PHOTODETECTORS

N. PAN
J. FAN

KOPIN CORPORATION
695 MYLES STANDISH BOULEVARD
TAUNTON, MA 02780

AUGUST 1997

FINAL REPORT FOR 09/01/1993 - 02/01/1997

THIS IS A SMALL BUSINESS INNOVATION RESEARCH (SBIR) PHASE II REPORT

MATERIALS AND MANUFACTURING DIRECTORATE
AIR FORCE RESEARCH LABORATORY
AIR FORCE MATERIEL COMMAND
WRIGHT PATTERSON AFB OH 45433-7734

NOTICE

USING GOVERNMENT DRAWINGS, SPECIFICATIONS, OR OTHER DATA INCLUDED IN THIS DOCUMENT FOR ANY PURPOSE OTHER THAN GOVERNMENT PROCUREMENT DOES NOT IN ANY WAY OBLIGATE THE US GOVERNMENT. THE FACT THAT THE GOVERNMENT FORMULATED OR SUPPLIED THE DRAWINGS, SPECIFICATIONS, OR OTHER DATA DOES NOT LICENSE THE HOLDER OR ANY OTHER PERSON OR CORPORATIONOR CONVEY ANY RIGHTS OR PERMISSION TO MANUFACTURE, USE, OR SELL ANY PATENTED INVENTION THAT MAY RELATE TO THEM.

THIS REPORT IS RELEASABLE TO THE NATIONAL TECHNICAL INFORMATION SERVICE (NTIS). AT NTIS, IT WILL BE AVAILABLE TO THE GENERAL PUBLIC, INCLUDING FOREIGN NATIONS.

THIS TECHNICAL REPORT HAS BEEN REVIEWED AND IS APPROVED FOR PUBLICATION.

Gail J. Brown

GAIL J. BROWN, Project Engineer
Sensor Materials Branch
Survivability & Sensor Materials Division

Robert L Denison

ROBERT L. DENISON, Chief
Sensor Materials Branch
Survivability & Sensor Materials Division

William R Woody

WILLIAM R. WOODY, Chief
Survivability & Sensor Materials Division
Materials & Manufacturing Directorate

Do not return copies of this report unless contractual obligations or notice on a specific document require its return.

REPORT DOCUMENTATION PAGE

Form Approved
OMB No. 0704-0188

1. AGENCY USE ONLY (Leave blank)	2. REPORT DATE	3. REPORT TYPE AND DATES COVERED
	AUG 1997	FINAL 09/01/1993--02/01/1997

4. TITLE AND SUBTITLE INGAP/GAAS QUANTUM WELL INFRARED PHOTODETECTORS

5. FUNDING NUMBERS
C F33615-93-C-5382
PE 35885
PR 3005
TA 05
WU 84

6. AUTHOR(S) N. PAN
J. FAN

7. PERFORMING ORGANIZATION NAME(S) AND ADDRESS(ES)
KOPIN CORPORATION
695 MYLES STANDISH BOULEVARD
TAUNTON, MA 02780

8. PERFORMING ORGANIZATION REPORT NUMBER

9. SPONSORING/MONITORING AGENCY NAME(S) AND ADDRESS(ES)
MATERIALS AND MANUFACTURING DIRECTORATE
AIR FORCE RESEARCH LABORATORY
AIR FORCE MATERIEL COMMAND
WRIGHT PATTERSON AFB OH 45433-7734
POC: Gail j. Brown, AFRL/MLPO, 937-255-4474 ext. 3238

10. SPONSORING/MONITORING AGENCY REPORT NUMBER
AFRL-ML-WP-TR-1998-4184

11. SUPPLEMENTARY NOTES PUBLIC RELEASE CLEARANCE
ASC-97-1497, 15 JUL 98

12a. DISTRIBUTION/AVAILABILITY STATEMENT
APPROVED FOR PUBLIC RELEASE; DISTRIBUTION IS UNLIMITED.

12b. DISTRIBUTION CODE

13. ABSTRACT (Maximum 200 words) THIS IS A SBIR PHASE II REPORT

THE OBJECTIVE OF THIS PHASE II SBIR WAS TO IMPROVE THE QUALITY OF MULTI-QUANTUM WELL MATERIALS SUITABLE FOR INFRARED DETECTOR APPLICATIONS AND TO INVESTIGATE NOVEL BANDGAP ENGINEERING CONCEPTS UTILIZING InGaP/GaAs HETEROSTRUCTURE MATERIALS. THE SUBCONTRACTOR, NORTHWESTERN UNIVERSITY, WAS SUCCESSFUL IN GROWING HIGH QUALITY InGaP/GaAs MULTIQUANTUM WELL MATERIALS BY LOW PRESSURE METAL-ORGANIC CHEMICAL VAPOR DEPOSITION (MOCVD), AND IN DEMONSTRATING IMPROVED PERFORMANCE IN THE PHOTODETECTOR TEST STRUCTURES FABRICATED FROM THESE MATERIALS. MOST OF THE RESULTS IN THIS REPORT ARE FROM THE RESEARCH WORK AT NORTHWESTERN UNIVIERSITY. THE PRIME CONTRACTOR, KOPIN CORPORATION, WAS NOT SUCCESSFUL IN TRANSFERING THE GROWTH PARAMETERS FOR THESE MATERIALS FROM NORTHWESTERN UNIVERSITY TO THEIR PRODUCTION-SCALE MOCVD REACTORS. NO REPORTABLE RESULTS WERE OBTAINED ON THE KOPIN MATERIALS.

14. SUBJECT TERMS	15. NUMBER OF PAGES
SBIR PHASE II REPORT PHOTODETECTORS, INFRARED, QUANTUM WELLS, INGAP, MOCVD	35
	16. PRICE CODE

17. SECURITY CLASSIFICATION OF REPORT	18. SECURITY CLASSIFICATION OF THIS PAGE	19. SECURITY CLASSIFICATION OF ABSTRACT	20. LIMITATION OF ABSTRACT
UNCLASSIFIED	UNCLASSIFIED	UNCLASSIFIED	SAR

EXECUTIVE SUMMARY

Most of the quantum well intersubband photodetector (QWIP) research has focused on multiple quantum well heterostructures of GaAs and $Al_xGa_{1-x}As$ due to the epitaxial growth and processing maturity of these materials. However, the magnitude of the dark currents in GaAs/AlGaAs QWIPs remained large for optimum connection to readout electronics, especially as the devices are extended to longer wavelength operation.[1] One way to improve the performance of these QWIPs is to replace the AlGaAs barrier with lattice-matched GaInP or GaInAsP alloys. The $Ga_xIn_{1-x}As_yP_{1-y}$ system has been investigated for the growth of lattice matched heterostructures of GaInAsP/GaAs ($1-y \approx 2.13x$) and GaInAsP/InP ($y \approx 2.2x$). Reviews of these systems have been published [2,3]. The quaternary composition range for lattice matched GaInAsP/InP includes the two optical fiber communication windows known today: zero dispersion at $\lambda = 1.3$ μm and minimum loss at $\lambda = 1.55$ μm [4,5]. Today, GaInAsP/InP lasers are the mainstay of optical communication systems.

The InGaAsP/GaAs material system did not develop as rapidly because it covered the same wavelength range as the $Al_xGa_{1-x}As$/GaAs material system, which was more widely developed. The AlGaAs/GaAs system was attractive because of its perfect lattice match to GaAs for all Al compositions. However, the lifetime of laser systems based on AlGaAs/GaAs laser diodes is limited by the laser diode lifetime due to problems connected with the presence of Al in the diode materials. High interaction of Al with oxygen leads to oxide formation at the mirror facet and enhances the non-radiative recombination of injected carriers near the mirror facet which creates the overheating of the mirror, and decreases the lifetime. Another lifetime limiting factor for AlGaAs-based laser diodes is the formation of dark-line defects, as a consequence of the spreading of the dislocations in the

active region during high-power operation. These problems have been solved by the replacement of AlGaAs with the Al-free GaInAsP/GaAs system. [6,7].

For use in QWIPs, lattice-matched GaAs-GaInP heterostructures have the advantages of an ultralow surface recombination velocity [8], very low interface roughness [9], an absence of the deep level traps associated with DX centers and oxygen defects in AlGaAs, and an order of magnitude higher electron mobility than AlGaAs [10]. These advantages are summarized in Table 1. below:

Table 1. Several Advantages of GaIn(As)P/GaAs over AlGaAs/GaAs

Characterization	GaInP/GaAs	AlGaAs/GaAs
Surface recombination velocity (cm/s)	1.5 cm/s	210 cm/s
[Reference]	J.M. Olsen, et.al. Solar Energy Inst. Appl.Phys.Lett.**55**	J.M. Olsen, et.al. Appl.Phys.Lett.**55**
Interface Roughness (ml of interface roughness necessary to fit mobility model of Sakaki et.al. for 20 Å well.)	< 1 ml	1-3 ml
[Reference]	W.C.Mitchel et.al. Air Force Wright Labs. Appl.Phys.Lett.**65.**	W.C.Mitchel et.al. Appl.Phys.Lett.**65.**
Electron Mobility (for undoped material)	780,000 $cm^2/V{\cdot}s$ at 4 K	71,000 $cm^2/V{\cdot}s$ at 4K
[Reference]	M.Razeghi et.al. Appl.Phys.Lett.**55**	P.Voisin et.al. Appl.Phys.Lett.**39**

Another disadvantage of AlGaAs is that the $Al_xGa_{1-x}As$ barriers become indirect gap semiconductors for $x > 0.4$. That is, if the Al concentration x is increased beyond x=0.4, the indirect X valley becomes the lowest energy gap. This has two undesirable effects: carriers in the barrier will be scattered from the X to Γ valleys during conduction, reducing the mobility, and carriers will be trapped in the quantum well in the longer-lifetime GaAs X valley. Such scattering and trapping will result in inefficient carrier collection and thus a poor responsivity.

Although such indirect barrier QWIPs have been fabricated[11], optimized direct-bandgap AlGaAs/GaAs QWIPs are limited to cutoff wavelengths of 5.6μm. Such a limitation does not exist in GaInAsP/GaAs. In a recent series of papers, the merits of valence band GaInAsP based QWIPs have been introduced. [12-15] The p-type (valence band) versions of these devices have shown photoresponse from 2 out to 7 microns at normal incidence and have demonstrated background limited photodetection up to sample temperatures of 120K.

These results have led to this present research into n-type (conduction band) QWIPs using GaIn(As)P/GaAs superlattices. The results of this research demonstrate long wavelength infrared (LWIR) photodetection using conduction band QWIPs. The potential revealed by these results is that the GaInAsP/GaAs material system can be used to produce monolithically integrated photodetectors with response from 3 to 30 μm using stacked superlattice layers of *n* and *p* type detectors. This is illustrated in Figure 1.

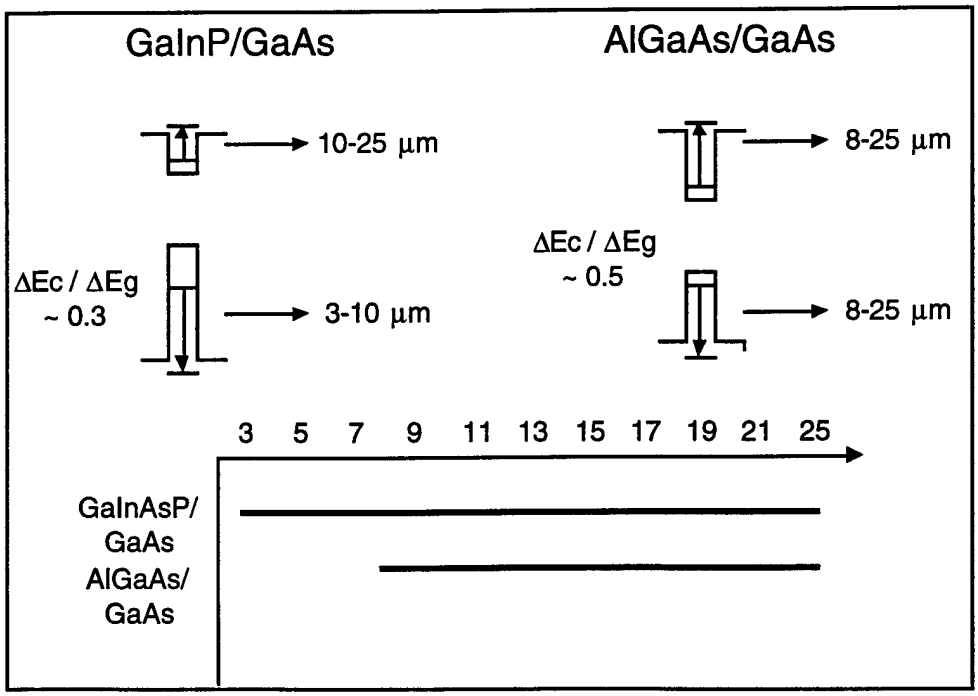

Figure 1. Infrared detection regions for InGaP/GaAs and AlGaAs/GaAs

QUANTUM WELL CHARACTERIZATION

Wafer characterization will be divided into electrical, optical and structural characterization techniques. For GaIn(As)P/GaAs based devices, the primary focus of the characterization is the experimental determination of the device parameters, i.e. the layer thicknesses and material compositions. Three instruments are used for structural characterization: the analytical x-ray diffractometer, the scanning electron microscope, and the transmission electron microscope (TEM). Cross-sectional transmission electron microscopy was used to measure the thicknesses of several GaInP/GaAs superlattices (100 Å GaAs/523 Å InGaP). A cross-section image of a 10 period superlattice is shown in Figure 2. Qualitatively the layers are very smooth without any apparent dislocations or interface layers.

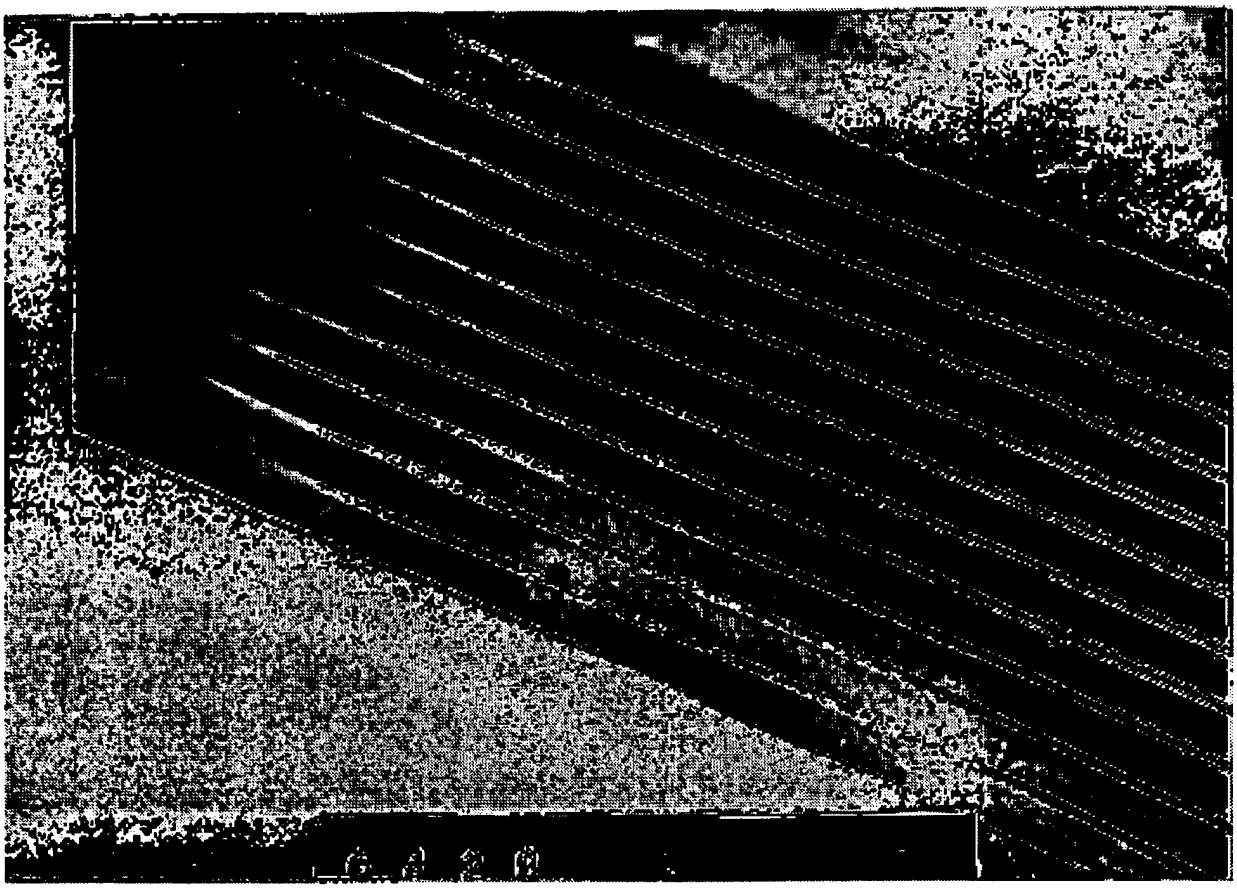

Figure 2. TEM photograph of a 10 period GaInP/GaAs superlattice.

Quantitative measurements of the thickness of the wells and barriers are possible by physically measuring the thicknesses on the photograph with a micrometer. Measurements for this sample yielded an average well thickness of 134 Å (standard deviation σ = 7 Å) and an average barrier thickness of 523 Å (σ = 8 Å). The variation in thickness was likely due to measurement error.

Advanced x-ray diffraction measurements and simulation of superlattices are used to "measure" the thicknesses of superlattice layers. X-ray diffraction spectra also measure the lattice mismatch between the substrate and epilayer(s) and give a quantitative measure of the film quality. A crystalline solid, consisting of a regular array of atoms, can be regarded as a natural three-dimensional diffraction grating for x-rays. Diffraction is governed by the Bragg equation:

$$\frac{2\sin\theta_B}{\lambda} = \frac{1}{d}$$

where Θ_B is complementary to the angle of incidence, and d is the spacing between two consecutive planes in the lattice. The wavelength of x-rays is of the order of 10^{-8} cm, whereas the smallest lattice periods lies in the range $10^{-8} \sim 10^{-5}$ cm. Accordingly, the scattering angles are large enough to be measured. For a typical rocking curve measurement, the sample to be characterized is rotated about the Bragg angle Θ_B, while the diffracted beam is measured. A typical x-ray diffraction measurement for a 1μm thick layer of GaInP grown on GaAs is shown in figure 3.

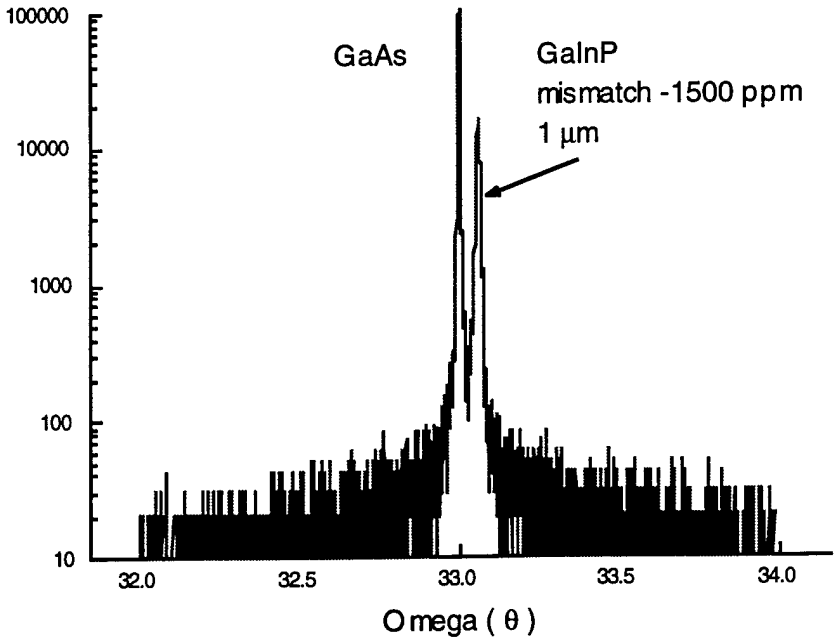

Figure 3. X-ray diffraction spectrum for GaInP/GaAs.

For materials like $Ga_xIn_{1-x}P$, the peak separation between the epilayer and the GaAs substrate can be used to determine the composition. The uniformity of the X-ray splitting performed on a 4 inch InGaP is shown in Figure 4. The energy gap is shown on the side of the figure. The uniformity across the wafer was very good. The variation in energy gap across the wafer was 1.875 ±0.003 eV.

More advanced dynamic x-ray scattering theory must be used to evaluate the x-ray diffraction spectra for superlattice samples. In multi-layer structures, interference fringes in the diffraction spectrum occur due to interaction between incident and reflected waves through different crystal layers, i.e. oscillations occur when two waves diffracted from different structures interfere with each other. The relation between the angular spacing of the fringes θq and the

InGaP 4"
X-ray Splitting

300K PL

1.8785 eV

1.8728 eV

1.8739 eV

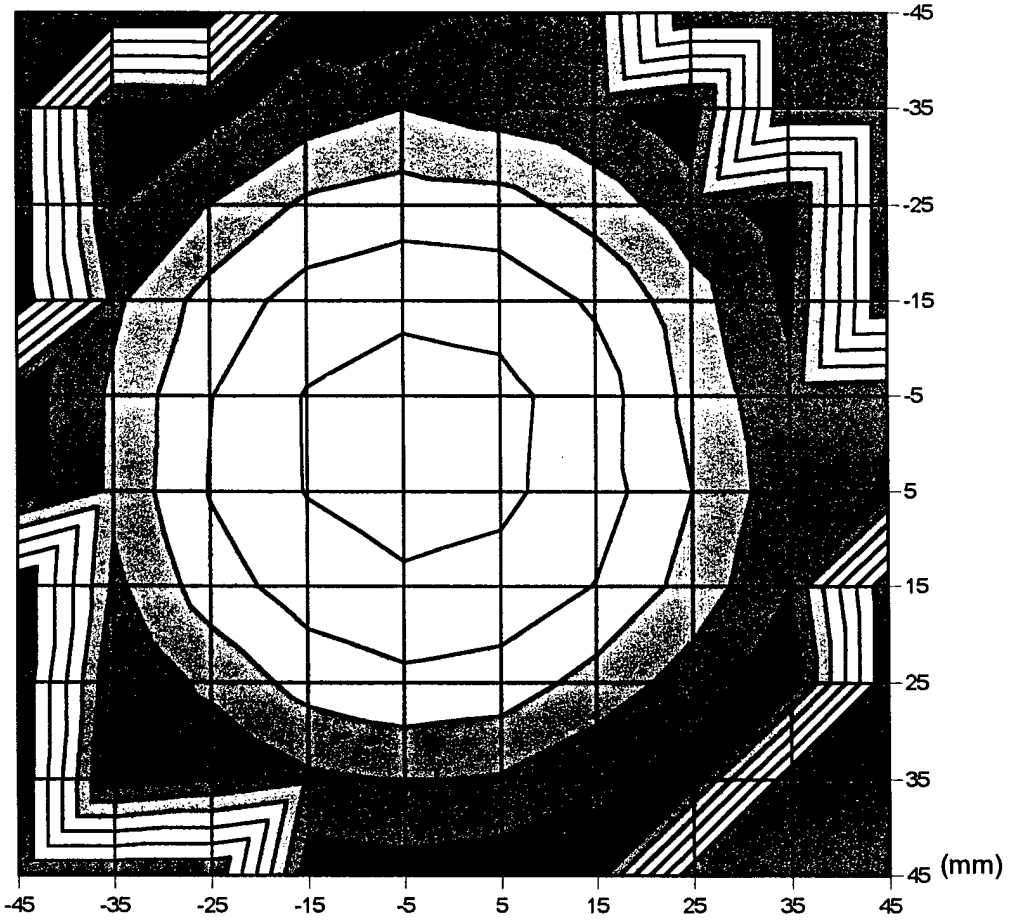

Major Flat

thickness L of the layer is

$$L = \frac{\lambda|\gamma|}{\Delta\theta \sin(2\theta_B)}$$

where $\gamma = \sin(\theta_B + f)$ and f is the angle between the crystal surface and the reflection plane. Thus, the applicable of this equation, combined with x-ray diffraction measurements of the wafer, allows the evaluation of the thickness of superlattice structures. In evaluating the superlattice samples, the choice of diffraction plane to study is important. The (004) reflection, being the point where all atomic planes within the sample scatter in phase, is the most commonly studied reflection for (001) oriented structures. For superlattice material containing GaAs, it is more revealing to study the (002) reflection. At the (002) point, alternating atomic planes within the sample scatter out of phase. For a high quality binary material like GaAs, where the average electron density of each atomic plane is very similar, the (002) reflection will be very weak. However, GaInP is a pseudo-random alloy of GaP and InP, and therefore the (002) reflection will not be as reduced. Therefore the (002) reflection will exhibit features predominantly from the GaInP aspect of the superlattice. The x-ray diffraction spectrum for the superlattice (123 Å GaAs/523 Å InGaP)

observed by TEM is shown in Figure 5.

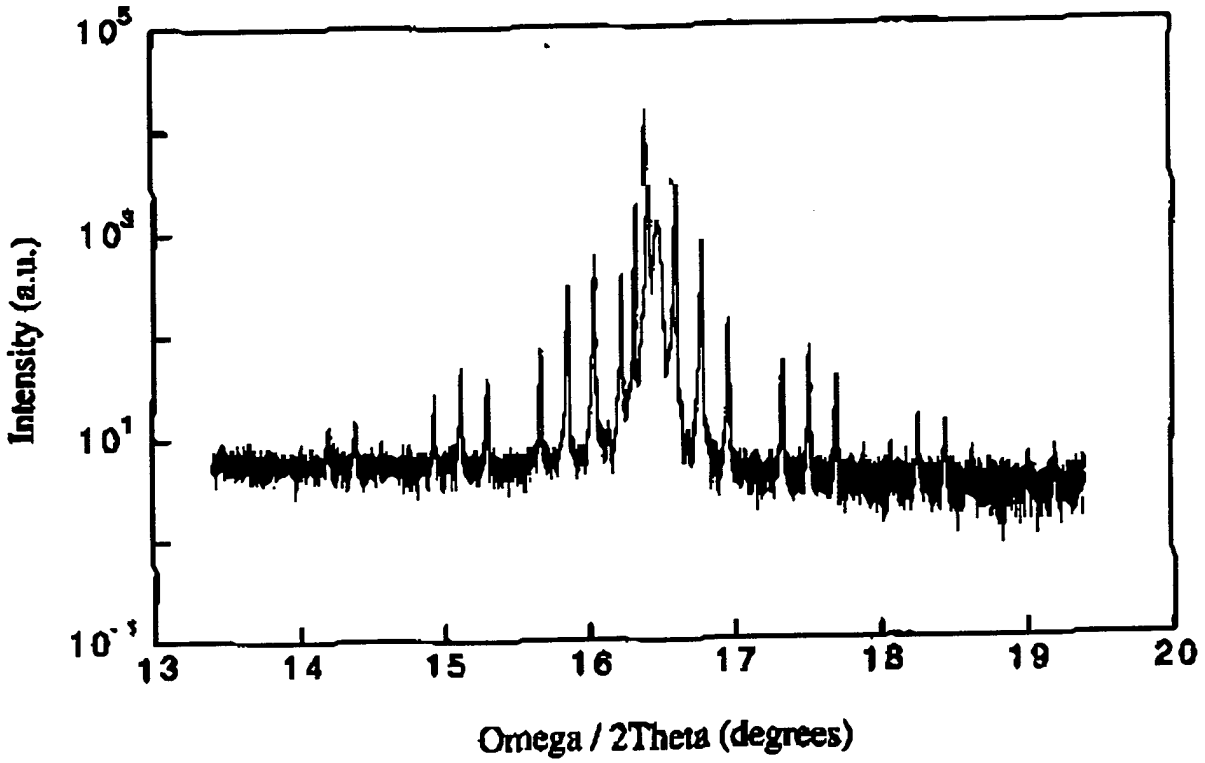

Figure 5 X-ray diffraction spectrum of 10 period (123 Å GaAs/523 Å InGaP) superlattice.

Analysis of the spacing between interference fringes in this spectrum yield average thicknesses of 123 Å for the GaAs wells and 523Å for the GaInP barriers. Comparison with the TEM measurement suggests the accuracy of thickness measurement by x-ray diffraction simulation to be ~ 10Å. Layer thicknesses measured for QWIPs fabricated and tested as part of this research were measured by x-ray diffraction, and have a similar accuracy. X ray diffraction for a 4 inch 335 Å InGaP/355 Å AlGaInP 10 period structure at two different positions across the wafer is shown in Figure 6. The spacing between the fringes were very close indicating excellent control of the thickness.

Fig 6.0

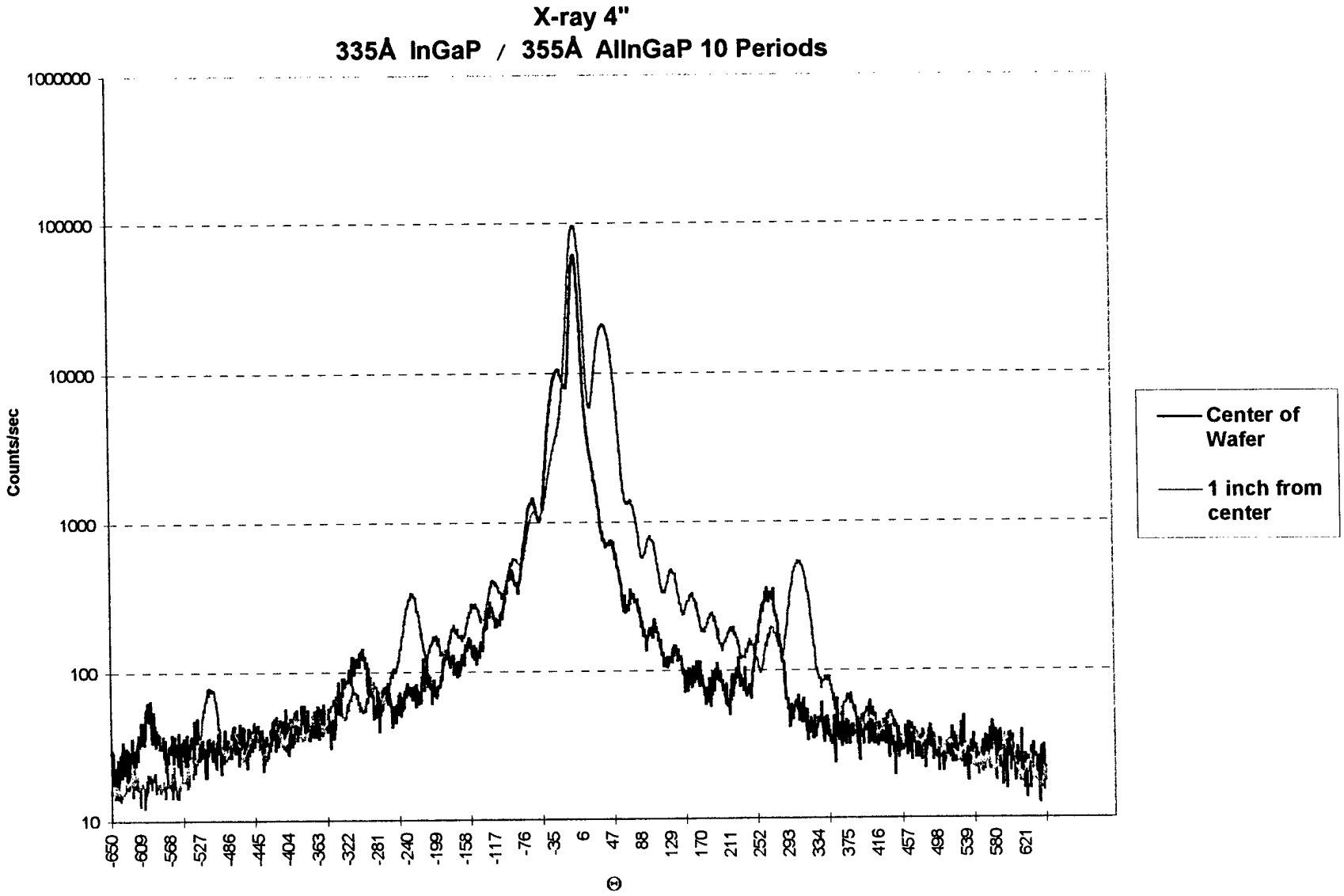
X-ray 4"
335Å InGaP / 355Å AlInGaP 10 Periods
1000000
100000
10000
1000
100
10
Counts/sec
-650
-609
-568
-527
-486
-445
-404
-363
-322
-281
-240
-199
-158
-117
-76
-35
6
47
88
129
170
211
252
293
334
375
416
457
498
539
580
621
Θ
Center of Wafer
1 inch from center

The slight shift in the peak position was due to the small shift in composition of the layers.

Wafers grown with the complete QWIP structure contain many more superlattice periods. The well thickness is also smaller than the above structure, resulting in a smaller angular spacing between fringes. The measured diffraction spectrum and a simulation for a 75 Å GaAs/500 Å InGaP QWIP is shown in figure 7.

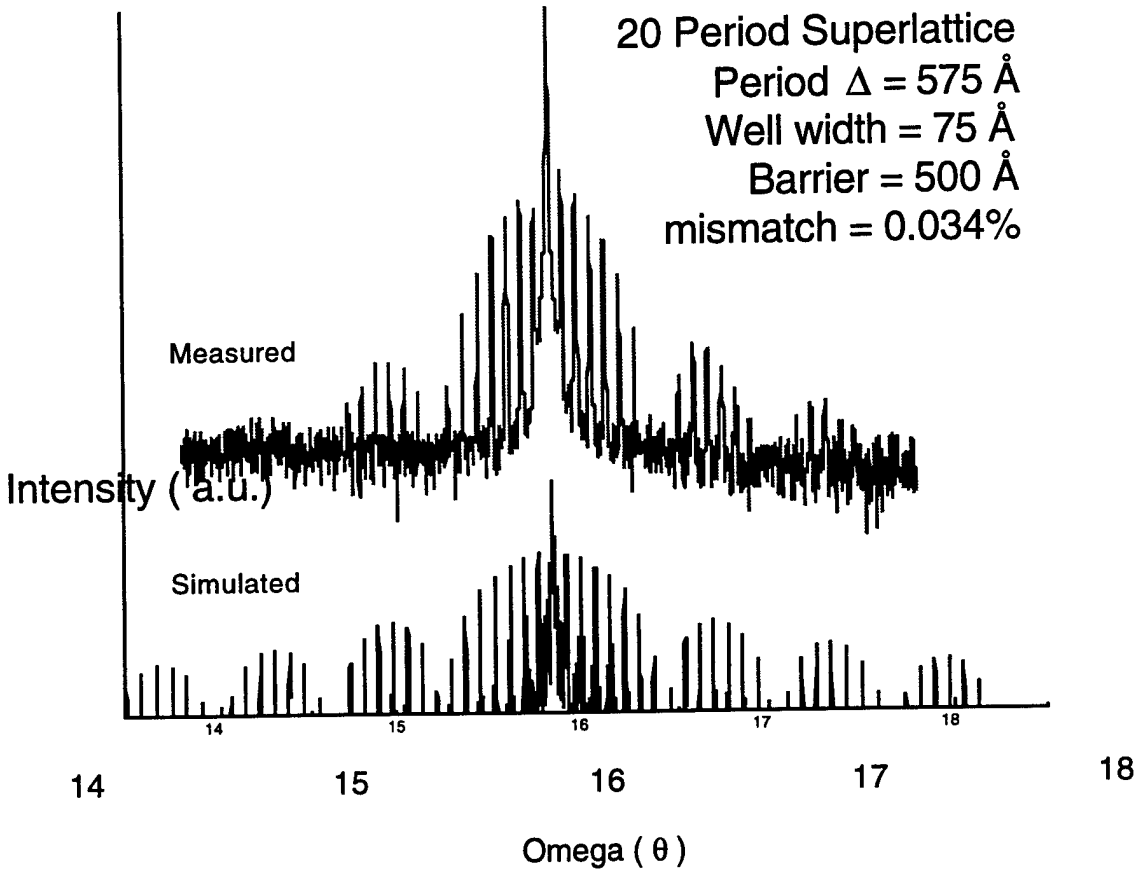

Figure 7. X-ray diffraction spectrum of QWIP structure.

Typically, scanning electron microscopy was used to view the topography of a surface, perhaps before and then after processing. However, the contrast in

scanning electron microscopy (SEM) is based in part on atomic number contrast, i.e. larger atoms produce more secondary electrons. Therefore it is possible to use SEM to view a cross section of a grown QWIP structure. A typical cross-sectional SEM image of a GaInP/GaAs superlattice is shown in figure 8. Because the SEM used in this research could not accurately measure the tilt angle of electron incidence, thickness measurements were not attempted from these images.

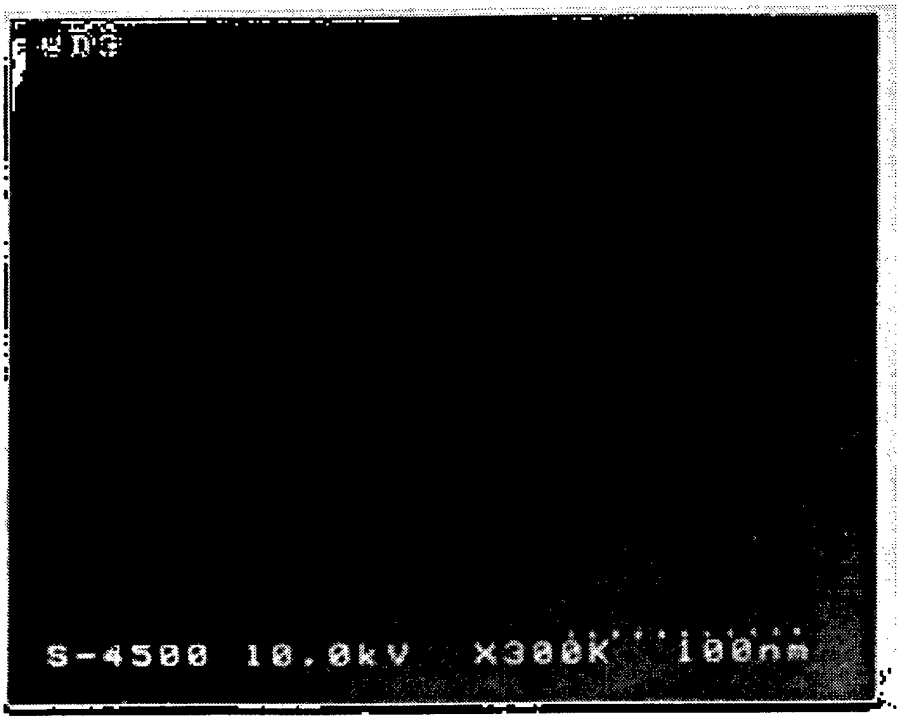

Figure 8. SEM image of the cross section of a GaInP/GaAs superlattice.

The scanning electron microscope was used extensively in evaluating the processing procedures used in detector fabrication. After photolithography, the etched mesas were imaged in order to determine the success of the mesa fabrication step before metallization was begun.

Photoluminescence (PL) is one of the most useful characterization methods for the semiconductor industry. Its most common use is the determination of bandgap for ternary and quaternary alloys, such as $Ga_xIn_{1-x}P$. Since the relation between the bandgap and composition x is known, a measurement of the bandgap can be inverted to determine x. PL is also sensitive to impurities, and PL spectrum peaks can be used to identify the type of impurity. In another use, the halfwidths of PL peaks are an indication of sample quality and crystallinity. PL spectrum presented in this proposal were measured using the 514 nm line of an Argon (Ar^+) ion laser, at sample temperatures from 77 - 300K, and excitation intensities of approximately 1 W cm^{-2}. Samples of $Ga_xIn_{1-x}As_yP_{1-y}$ were grown with varying compositions x and y such that they covered the entire range of compositions from GaAs to GaInP. The result is shown in Figure 9.

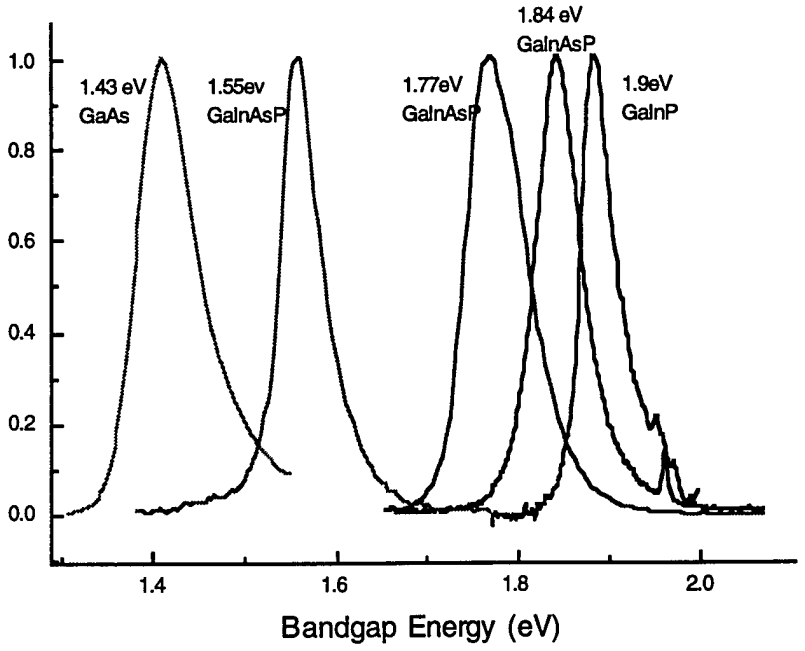

Figure 9. 300 K Photoluminescence of $Ga_xIn_{1-x}As_yP_{1-y}$ for varying compositions.

Most textbooks on quantum mechanics solve a simple problem of one dimensional motion of a particle confined to a quantum well. When the well size becomes smaller than the spatial extent of the particle wavefunction, the energy of the particle becomes quantized and it increases with the decreasing well size. This behavior arises directly from the uncertainty principle. The energy levels of the carriers can be measured by optical techniques such as photoluminescence. The measured energy shift, compared to the bandgap energy of the well material, is often referred to as the quantum-confinement shift. The room temperature photoluminescence spectrum for a QWIP wafer with 67Å GaAs wells and 500 Å GaInP barriers is shown in figure 10 along with a spectrum of pure GaAs for comparison.

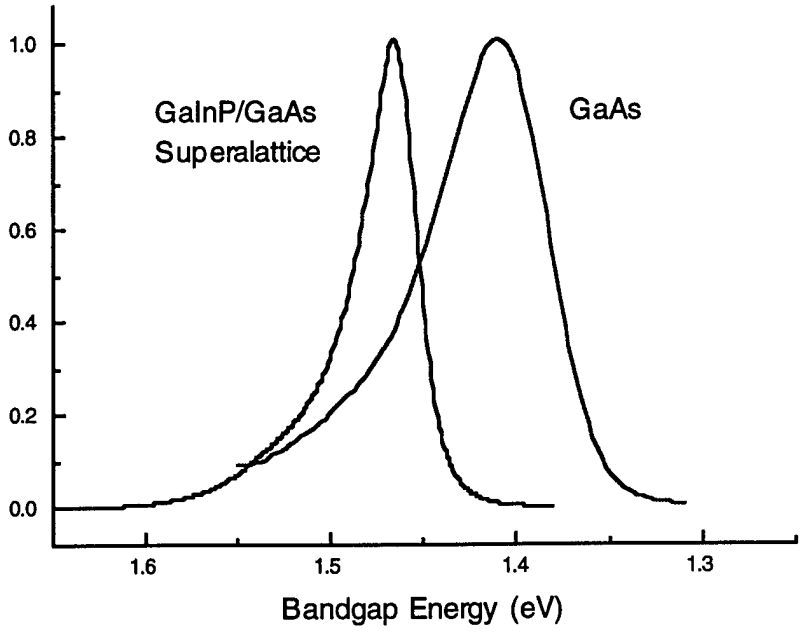

Figure 10. Photoluminescence of QWIP wafer illustrating confinement shift.

Photovoltage spectroscopy (PVS) measures the open-circuit voltage response of the semiconductor sample as a function of the wavelength of the incident

radiation. This open-circuit photovoltage is proportional to the absorption coefficient of the material measured, and gives us the same absorption profile as an absorption/transmission measurement. PVS measurements were performed using a Biorad PVS system. A junction is made between a transparent electrolyte and the semiconductor on the epilayer side, and an ohmic contact is made to the substrate side of the sample. Figure 11 shows the room temperature PVS of a ten period superlattice of GaInP/GaAs consisting of 200Å GaInP barriers and 55 Å GaAs wells. The well resolved peaks corresponding to transitions from the first conduction band subband to the first heavy hole subband (E1HH1) and first conduction band sublevel to the first light hole subband (E1LH1) are observed.

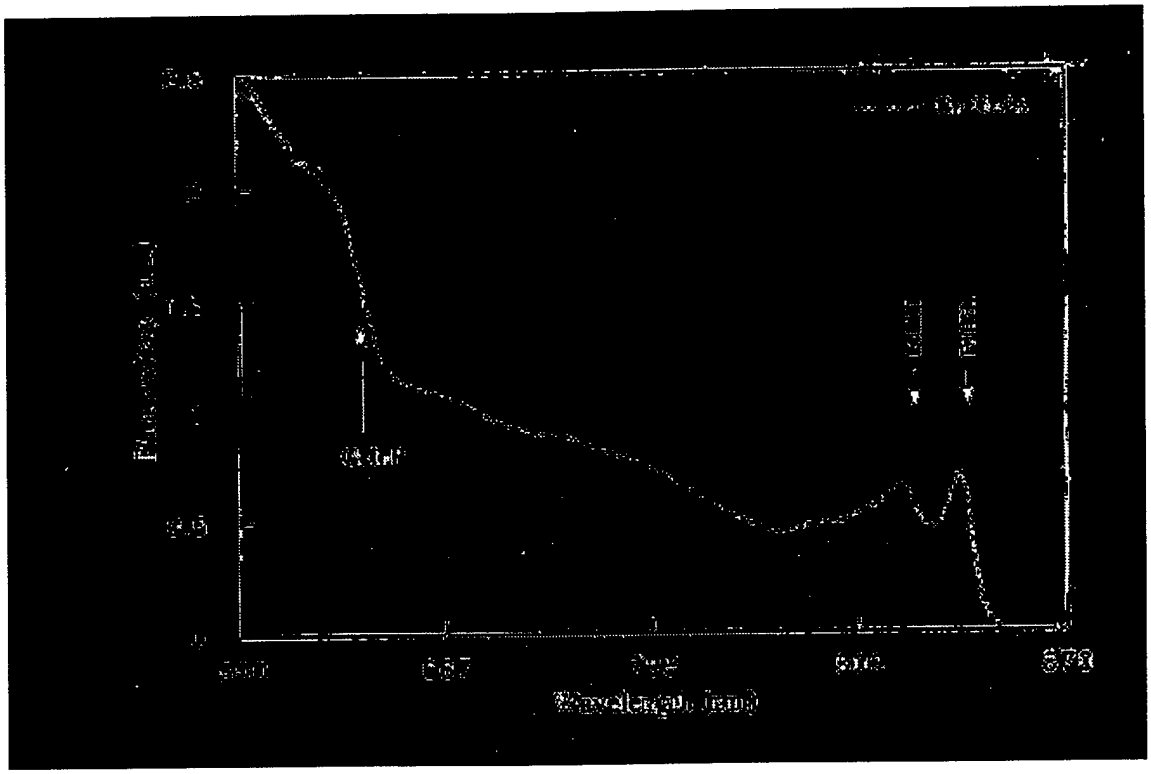

Figure 11. PVS measurement of ten period GaInP/GaAs superlattice.

By using a model of the quantum well (such as the Kronig-Penny model), the energy levels in the conduction and valence band quantum wells can be computed and compared to the experimental measured values. A simple calculation like the

Kronig Penny model requires only the bandgaps and effective masses of the well and barrier materials, as well as the band-offset ratio.

For the following values:

E_g GaInP = 1.89 eV

E_g GaAs = 1.42 eV

GaAs: $m_c=0.0667m_o$, $m_{hh}=0.475m_o$, $m_{lh}=0.087m_o$

GaInP: $m_c=0.1175m_o$, $m_{hh}=0.660m_o$, $m_{lh}=0.145m_o$.

$DE_c/DE_g = 0.3$

The Kronig-Penny model predicts two allowed transitions at 1.482 and 1.520 eV (as observed in figure 11) for a well width of 58Å and barrier width of 190Å. These results are summarized in Table 2.

Table 2. Simulation of PVS results using Kronig-Penny model

	Well (Å)	Barrier (Å)	E1HH1 (eV)	E1LH1 (eV)
Kronig-Penny	58	190	1.482	1.520
PVS/X-ray data	55	200	1.483	1.520

FABRICATION AND TESTING of QWIP

To meet the high specifications required, the GaInP/GaAs QWIPs had to be optimized for three different aspects: material and quantum well structure, efficient light coupling, and depression of the dark current and therefore noise current. Only one previous publication[16] exists for GaInP/GaAs QWIPs, and it reported results for only one sample. In this proposal, the optimization of the material and quantum well structure to have the high performance in the required spectral region is demonstrated.

Systematic measurements were made on three samples. The samples differ only in their quantum well structure (i.e. well width). Temperature dependent dark current and dynamic resistance measurements as well as noise, photocurrent, and spectral responsivity measurements are combined in order to analyze in detail the relationship between the QW structure and device performance.

A series of GaInP/GaAs *n*-type (conduction band) QWIP samples was grown in order to evaluate the potential for GaIn(As)P/GaAs QWIPs photodetectors to provide significant performance improvements over AlGaAs/GaAs QWIPs for the wavelength range from 10 - 25 μm. The optical, electrical, and structural characteristics of these samples are presented in Table 3:

Table 3. Properties of test GaInP/GaAs samples.

Sample	Sample1	Sample2	Sample3
GaAs Well width (Å)	40	67	75
GaInP Barrier width (Å)	492	510	505
Da/a mismatch (ppm)	400	-490	-875
300K PL peak (eV)	820	835nm	845

A quantum well infrared photodetector is a unipolar device on which two contacts must be made. Since the structure is grown on a semi-insulating substrate to permit backside illumination while avoiding free-carrier absorption, the two contacts must both be made on the front face of the device. Therefore, mesas must be controllably etched down to the bottom contact layer. If the etch depth is not deep enough, metallization will be made to the superlattice. Similarly, if the whole bottom contact layer is etched away, no contact can be made through the insulating substrate.(Fig. 12)

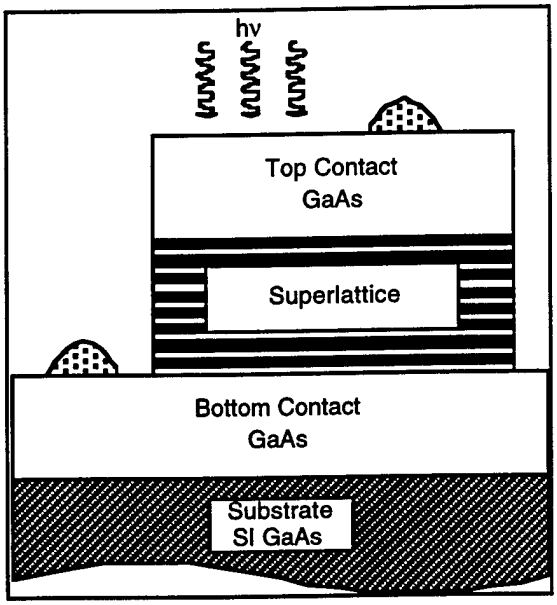

Figure 12: Cut-away of a mesa structure for front face contacting.

Etching of QWIP structures can be difficult due to the large depths which must be removed. For instance, an n-type GaAs/$Ga_{0.51}In_{0.49}P$ QWIPs can be expected to have 60 Å wide wells, 500 Å wide barriers and a 0.5 μm top contact layer. For a 50 period QWIP, this means an etch depth of 50*(60 Å +500 Å) + 500 Å + 0.5 μm = 3.35 μm. An etch mask must be capable of withstanding a great deal of stress, both chemically and mechanically. Simple photoresist masks were attempted at first. However, the photoresist was not mechanically stable

enough on its own to resist a long selective etch in mineral acids. Silicon Dioxide grown by either Plasma Enhanced Chemical Vapor Deposition (PECVD) or Electron Beam Evaporation (E-beam) proved to be much more resistant to undercut. However, pinholes are formed in the evaporation process which allow undesired etching of the mesas. Moreover, the metallization step can then fill these etched holes and short out the mesas. The solution to the etch mask problem was to use both photoresist and SiO_2. The silicon dioxide provides the strength and the photoresist fills the pinhole. The probability of undesired etching of the mesas is thus greatly reduced. Therefore, the procedure for obtaining the etching mask is as follows: (i) deposition of an SiO_2 layer over the whole sample area, (ii) photolithography to define square patterns of photoresist, and (iii) etching of the SiO_2 layer using a buffered hydrofluoric acid solution. Typically, 400 μm x 400 μm mesas are used for evaluation of single element QWIPs.

In conventional GaAs/$Al_xGa_{1-x}As$ QWIPs, mesas can be wet chemically etched using a non-selective etchant such as 1 H_3PO_4 : 1 H_2O_2 : 8 H_2O, which provides a controllable etch rate of about 0.8 μm/min. for both GaAs and $Al_xGa_{1-x}As$. In GaAs/$Ga_{0.51}In_{0.49}P$ heterostructures, we have investigated non selective etchants based on H_2SO_4 : H_2O_2 : H_2O and Br_2 : MeOH. In both cases, the etch rate was difficult to control because of the difference in the etch rate of GaAs and $Ga_{0.51}In_{0.49}P$ ($Ga_{0.51}In_{0.49}P$ is much slower than GaAs). Therefore, a fully selective etching procedure was investigated. 1 H_3PO_4 : 1 H_2O_2 : 10 H_2O (1:1:10) was used as the GaAs etchant, and undiluted HCl was used as the GaInP etchant. Both etchants are highly selective. The top GaAs contacts layer were first removed by the phosphoric acid-based etch. The superlattices were then etched away by successive etches in the following manner:

1. 20 seconds in HCl (barrier etch or $Ga_{0.51}In_{0.49}P$ etch)
2. 10 seconds of deionized water rinse

3 20 seconds in 1:1:10 (well etch or GaAs etch)

4 10 second of deionized water rinse

This procedure was found to be highly controllable and reproducible for GaAs/ $Ga_{0.51}In_{0.49}P$ superlattices. Upon mesa etching, the SiO_2 + photoresist etch mask is removed by soaking the sample into concentrated HF which etches the SiO_2 layer and lifts off the photoresist layer.

Following mesa etching and mask removal, two metallization techniques have been used successfully. These procedures had been developed and optimized for aluminum-free high power lasers. The first technique consists in the deposition of Au/AuZn/Au by thermal evaporation over the whole sample area. Following the evaporation, the sample is then pre-annealed at a temperature of 330 C under a flow of forming gas (a mixture of 10% hydrogen in nitrogen) for 2-3 minutes in order to improve the adhesion of the metallization layer. 100 μm x 100 μm photoresist squares are then patterned at the top and bottom of the etched mesas using standard photolithography procedures. The Au/AuZn/Au is then etched away using a KI : I_2 : H_2O solution, and the photoresist mask is then dissolved in acetone. The Au/AuZn/Au metallization is then annealed at 440 C under forming gas for 2-3 minutes.

Figure 13 shows a top view of 4 mesas after etching and metallization. Once the samples were fully processed, individual chips were cleaved off and mounted onto copper heat sinks. Here again, the mounting procedure was derived from previous developments and optimizations performed for high power lasers, except the mounting requirements are far less stringent for QWIPs. The chips were indium-bonded to copper heat sinks, and connections were made using a ball-bonder apparatus equipped with 25 μm diameter gold wire.

Since the goal of the initial series of samples was to demonstrate very long wavelength detection, the photoresponse spectrum is the most critical measurement of the performance of these devices.

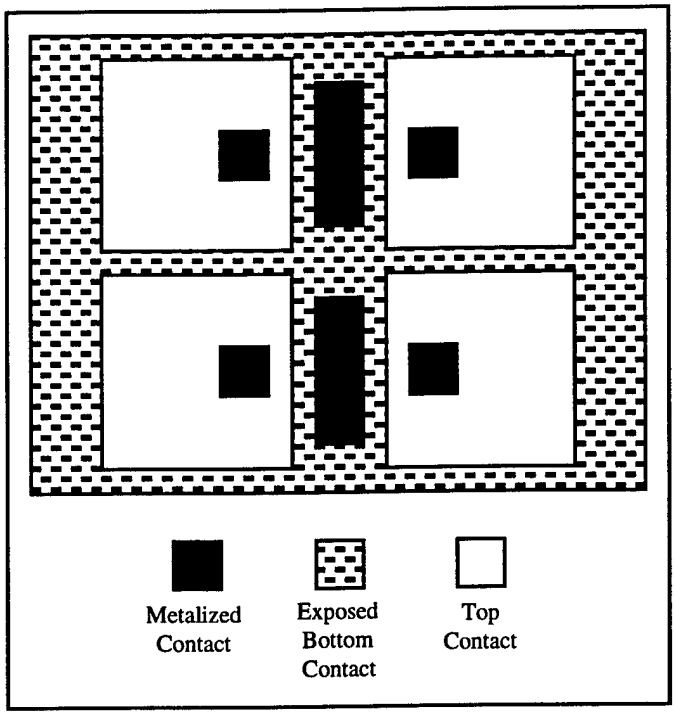

Figure 13: Top view of etched sample

The responsivity wavelength spectra R(l) of the samples was measured at normal incidence using a Mattson Fourier-transform infrared (FTIR) spectrometer. The spectrometer uses a pyroelectric detector which has a flat response over the range of 2 to 25 μm. The normalized responsivity spectra R(λ) for three samples is shown in Fig. 14. These samples clearly demonstrate the high controllability and accuracy of the MBE grown QWIPs even for very long wavelengths. Table 4 contains the measured values of peak λ_p and cutoff λ_c wavelength, full width half maximum ($\Delta\lambda$), as well as the peak responsivity values. Figure 15 shows the peak wavelength plotted against the well width and Figure 16 shows the normal incidence responsivity versus bias.

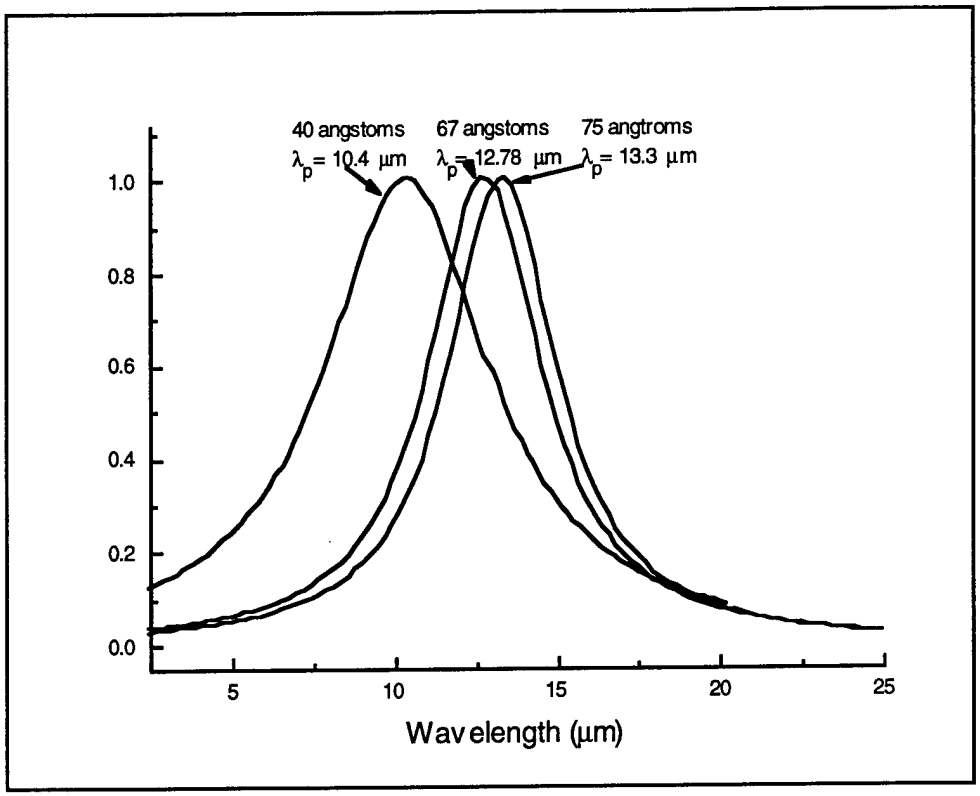

Figure 14. Normalized Optical Response at 77K

Table 4. Peak responsivities in A/W (at -4 V and 78K) for the different samples as well as the peak and cutoff wavelengths and FWHM $\Delta\lambda$ (in $\Delta\lambda$ and meV)

Sample	1	2	3
λ_p	10.4	12.78	13.3
λ_c	13.4	14.85	15.34
$\Delta\lambda$	6µm	4.25µm	4.1µm
	185 meV	37 meV	42 meV
Rp (A/W)	0.002	0.04	0.07

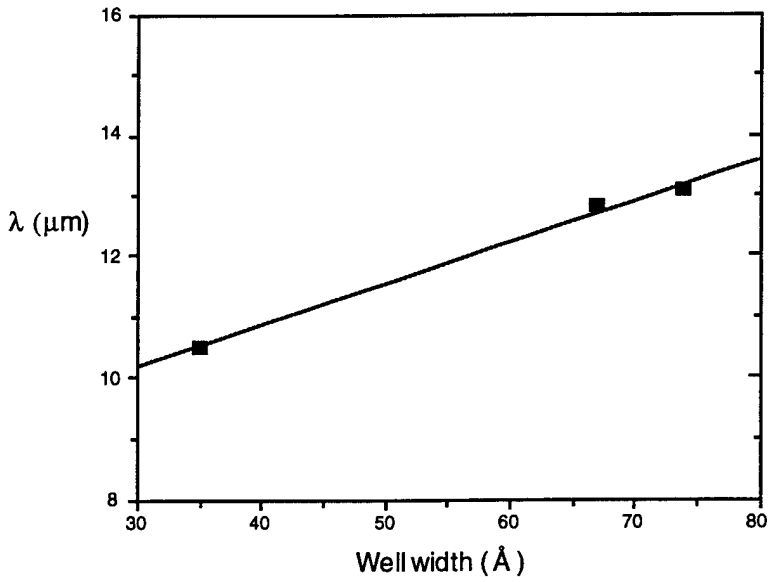

Figure 15. Peak wavelength as a function of well width.

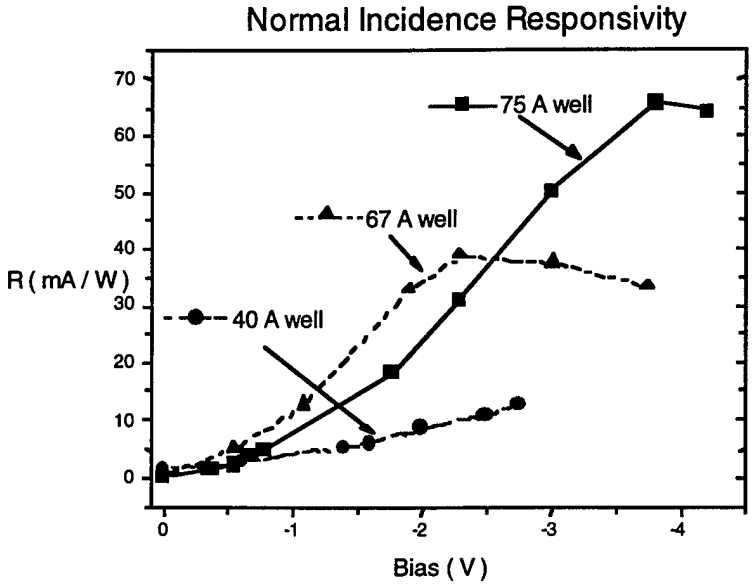

Fig. 16 Peak normal incidence responsivity vs. bias for the different samples.

The dark current i_D play a crucial roll in determining the ultimate performance of the individual detectors in the array. Therefore, detailed measurements of the

temperature dependence of the dark current versus voltage were made using a cold shield that completely surrounded the QWIP and had the same temperature. Figure 17 shows the temperature dependence of the dark current-voltage curve for sample 2. For this sample, thermionic emission is the dominant carrier mechanism down to ~ T=-30K, which is evident by the exponential decrease of the dark current with temperature.

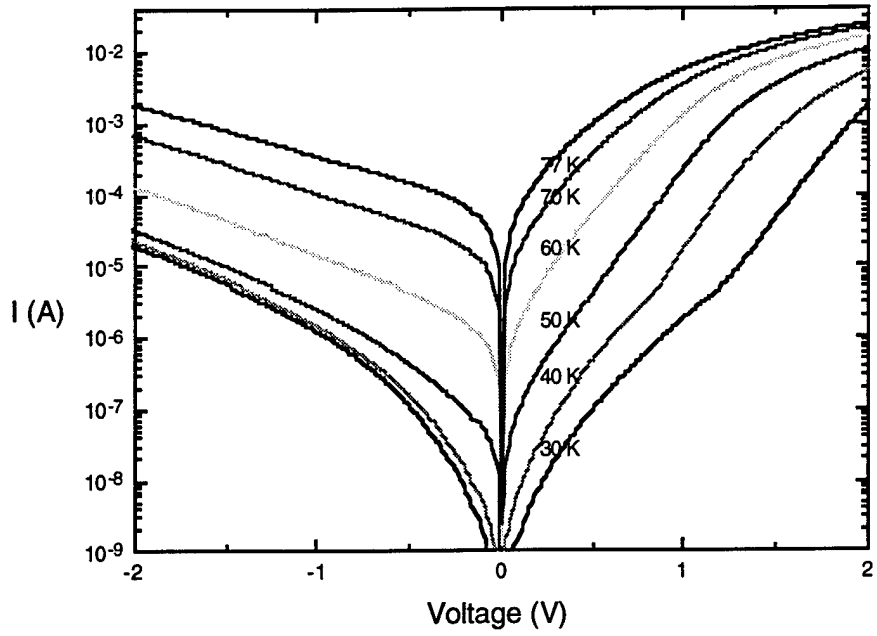

Figure 17. Current-voltage (I-V) curve for sample 2 at different temperatures.

In order to more clearly observe the exponential dark current behavior with bias and temperature, the date was replotted as a function of 1/T for different biases. This is shown in figure 18 for sample 2. It is evident that for low biases up to -3 V and high temperatures, thermal activation determines the dark current due to the thermionic emission of electrons from the well. This region is represented by the straight line in the plot of $\log(I_D)$ vs 1/T down to T = 40K. The flat part of

the curve is due to the onset of tunneling, (which occurs at T < 40 K). At low bias (where tunneling is negligible) the dark current is expected to increase exponentially with temperature following:

$$I \propto T \exp\left(-\frac{\Delta E}{kT}\right)$$

with the thermal activation energy given by $\Delta E = E_c - E_F$, where k is Boltzmann's constant and T is the absolute temperature in Kelvin. In order to examine this dependence in detail, the current-voltage curves of all three samples were replotted in Figure 19 for V_b = -0.1 V as log (I_D/T) vs. 1/kT. As expected, the

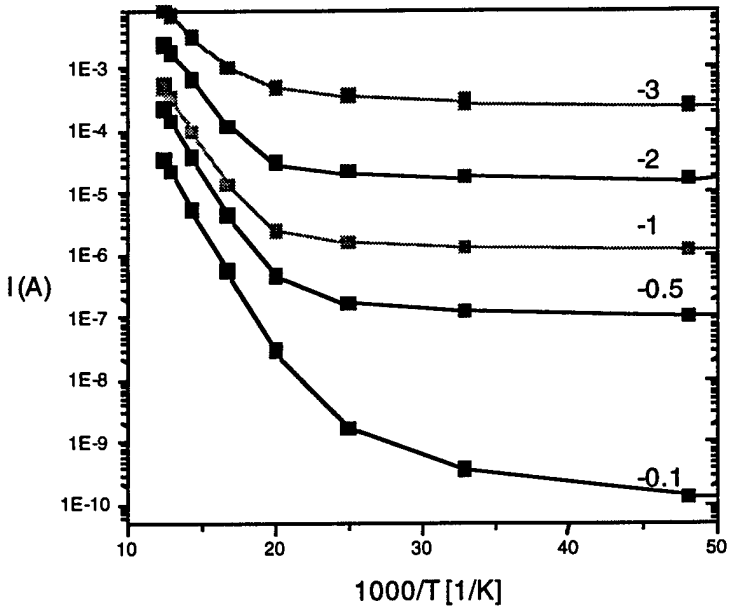

Figure 18. Dark current vs. inverse temperature of sample 2 for different bias, the straight lines represent the thermally activated dark current while the leveling off at low temperature in due to tunneling.

normalized dark current log (I_D/T) plotted against inverse temperature follows an excellent straight line for all the sample and from the slop of this line we determine ΔE.

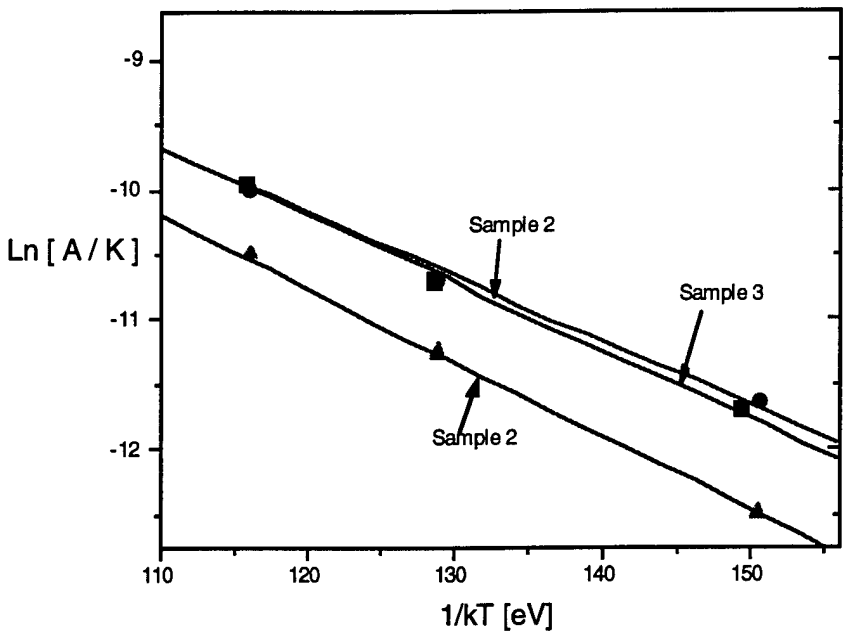

Figure 19. Normalized dark current (A/K) versus 1/kT showing the thermal activation of the dark current.

Based on the responsivity measurements discussed above, the cutoff wavelength λ_c was determined for each sample and the corresponding cutoff energy E_c determined from $E_c = hc/\lambda_c$ where h is Planck's constant and c is the speed of light. The Fermi level E_F of the two dimensional electron gas in the well can be obtained from:

$$N_D = n_o \ln\left(e^{E_F/kT} - 1\right)$$

and

$$n_o \equiv m^* kT / \pi h^2 L_w$$

where N_D is the effective doping density in the well, m* is the electron effective mass, and L_W is the well width. Bandara et.al have shown the electron-electron exchange interaction effect to be significant in long wavelength intersubband detectors [17]. For doping of for $N_D = 5 \times 10^{17}$ cm^{-3}, the Fermi energy obtained from these calculations is E_F = 29 meV, 28 meV, 25 meV for the 75Å, 65Å, and 40Å wells respectively, and the exchange interaction is 27 meV, 22 meV, and 19 meV for the 75Å, 65Å, and 40Å wells respectively. Combining E_C with the Fermi and exchange energies obtained from these calculations, $\Delta E = E_c - E_F - E_{EXCH}$. ΔE is determined for all three samples and is compared in Table 5 to the values obtained from the slope of the dark current curves in Figure 19. As can be seen from the table, there is very good agreement between the values obtained from the spectra (λ_c) and that obtained from the dark current measurements assuming thermal activation in this temperature range.

Table 5. Activation energy as obtained from the normalized dark currents vs 1/T slope (upper row) and by the cutoff energy and exchange and Fermi level calculations (lower row).

Sample	1	2	3
ΔE (meV) I-V	48.57	55.69	51.59
ΔE (meV) calc.	48.5	55.5	51.83

The dynamic resistance which is governed by the same mechanisms as the dark current plays a crucial role for coupling the focal plane array to the readout circuits. For typical CMOS readout circuits a detector output impedance of more than 1 MΩ is needed in order to work in the direct injection mode [18] without buffer circuits and electronic choppers. Figure 20 shows the dynamic resistance at -2 V for sample 2 with 400 x 400 μm^2 mesas as a function of inverse

temperature (1/T). As with the dark current a straight line is evident for temperatures above 50K. The effect of tunneling can be seen by the tendency towards saturation at low temperatures. It can be seen that 1 MΩ and higher output impedances can be achieved by cooling the sample to ~ 60K. In this temperature range most of the Si based multiplexors can work without any modification in a direct injection mode.

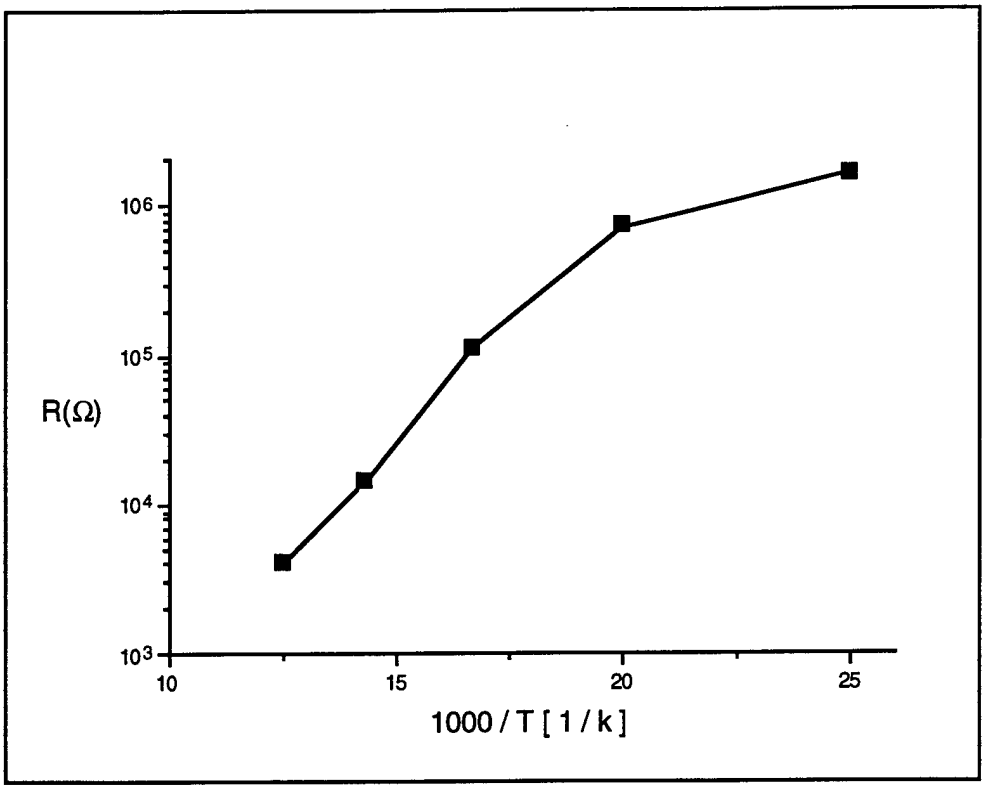

Figure 20. Dynamic resistance vs. reciprocal temperature at -0.5 V for sample 2.

The noise was measured at 80K using an EG&G lock-in amplifier. The noise was measured under dark conditions (i.e. a cold shield surrounding the QWIP). Since at 80K the samples are not BLIP, the dominant noise mechanism is shot noise. Figure 21 shows the bias dependent shot noise at 80K for sample 3.

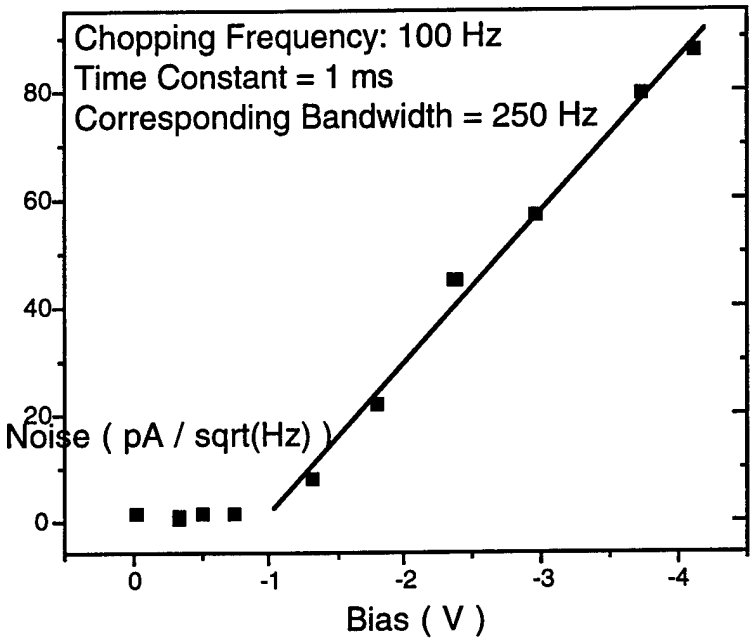

Figure 21. Noise current measured for sample 2.

The noise gain of the device at these temperatures can be calculated from the noise current and the dark current of the device at that temperature, using the following equation:

$$I_n = \sqrt{4qI_d G\Delta f}$$

where I_d is the dark current of the device, G is the noise gain, and Δf is the bandwidth. For a sufficiently high bias , the quantum well capture probability p_c will be << 1, so that the ratio of the noise gain to the photoconductive gain can be assumed to be unity[19]. Hence the measured gain from this noise measurement is also the photoconductive gain. As expected, the noise increases superlinearly with bias. The optical gain was determined from the noise and dark currents as a function of bias. . Figure 22 shows the bias dependent optical gain at 80K for sample 3. The gain increases with bias, with a plateau at -1.5 V at gain = 0.25,

and then increases rapidly with the bias. For a 20 period superlattice structure, gain of 0.25 is equivalent to a hot electron mean free path of 5 QW periods, i.e. around 3500Å, and therefore corresponds to a capture probability of p_c=0.2. For V> 2 V, the superlinear increase in gain is due to avalanche multiplication of the high energy electrons.

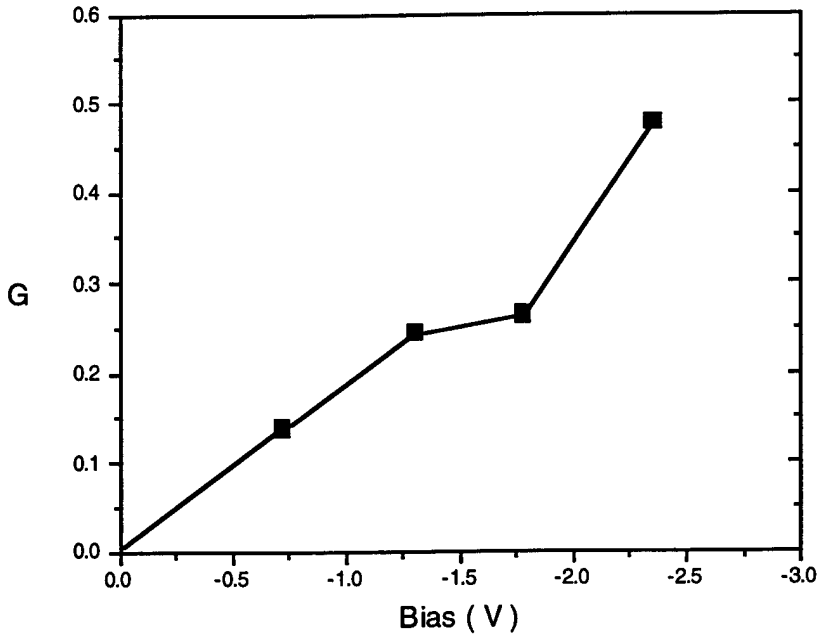

Figure 22. Optical gain, determined from the measured dark current noise for sample 3.

The responsivity of the detector can be expressed in terms of its quantum efficiency (h) and gain G as:

$$R(\lambda) = \eta G \frac{q\lambda}{hc}$$

From this equation, a quantum efficiency of 1.3% is calculated for sample 3 using values at -2.5V: gain = 0.50, R(λ) = 0.072 A/W, and λp = 13.3 μm.

Combining the responsivity values and the noise currents, the specific detectivity D* can be obtained from:

$$D^* = \frac{R_p}{i_n}\sqrt{A\Delta f}$$

Figure 23 shows the bias dependence of D* for sample 3 at 80K. D* increases with bias up to -0.75V, and then saturates. Although the responsivity continues to increase with bias at higher voltage, the noise also increases and so the detectivity remains constant.

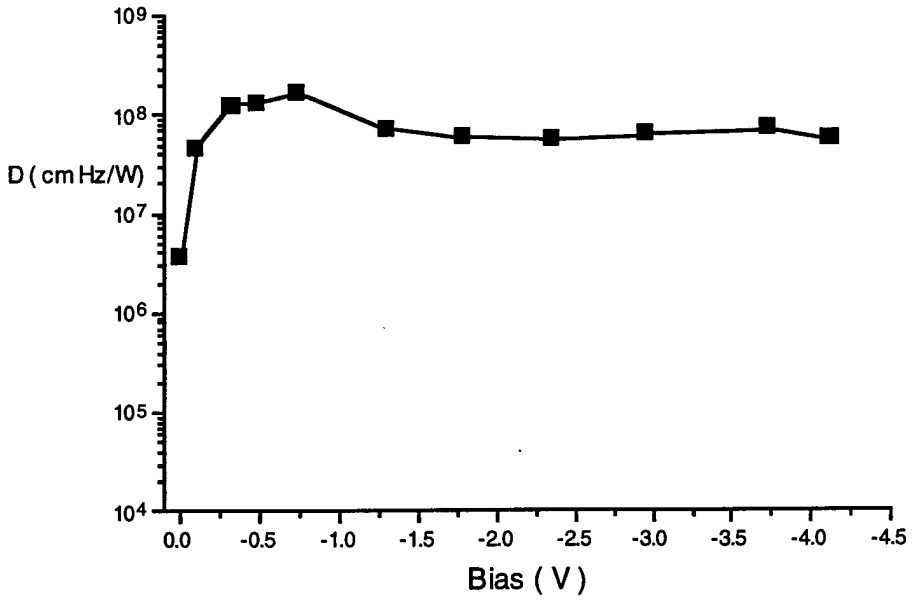

Figure 23. Detectivity (D*) as a function of bias for sample 3 at 80K.

Several favorable comparisons can be made between these preliminary detectors and AlGaAs detectors already published in the literature.

Table 7. Comparison of GaInP and GaAlAs QWIPs.

Value	GaInP/GaAs sample 2	AlGaAs/GaAs ref. Levine JAP 76 1994	AlGaAs/GaAs ref. Levine JAP 70 1991
J_{dark} [$\mu A/cm^2$] at -1V, 50K	1875$\mu A/cm^2$	2546 $\mu A/cm^2$	3183 $\mu A/cm^2$
Gain (-1.5V, 77K)	0.25	0.1	.065

The detectivity of these preliminary samples, which were not optimized, also compares well with the expected values for detectivity as a function of cutoff wavelength. In summary, in this study experimental results characterizing GaInP/GaAs -based very long wavelength quantum well infrared photodetectors in the 10-15 μm spectral range have been presented. As was emphasized throughout the work, these were preliminary experiments intended to show the opportunity for GaIn(As)P/GaAs QWIPs to be used instead of AlGaAs/GaAs QWIPs for long wavelength photodetectors. Further optimization of these GaInP/GaAs detectors is necessary, in addition to the growth and fabrication of GaInAsP/GaAs QWIPs for even longer cutoff wavelengths.

References

1. J.Y. Andersson, J. Appl. Phys. **78**, 6298 (1995).

2. B.A.Wilson, IEEE J. Quantum Electron. **24,** 1763 (1988).

3. P.Ho, et.al. Appl. Phys. Lett. **62,** 93-95 (1993).

4. M. Razeghi, *MOCVD Challenge vol 1*. IOP publishers, 1989.

5. M.Razeghi, *MOCVD Challenge vol 2* IOP publishers, 1995.

6. M. Razeghi, Nature **369** 631(1996).

7. Garbuzov et.al. IEEE J. Quantum Electron. **QE-27** 1531.

8. J.M. Olson et.al. Appl. Phys. Lett. **56,** 623 (1990).

9. W.C. Mitchel et.al. Appl. Phys. Lett. **65,** 1578 (1994).

10. M. Razeghi et.al. Appl. Phys. Lett. **55,** 457 (1989).

11. B.F.Levine et.al. Appl. Phys. Lett. **58**, 1551 (1991).

12. J. Hoff et. al. Appl. Phys. Lett. **67,** 22 1995.

13. J. Hoff et. al. Appl. Phys. Lett. **78** 2126 1995.

14. J. Hoff et. al. Superlatt.&Microstruc.**18,** 249 (1995)

15. J. Hoff et. al. SPIE Proc. **2685,** 62 (1996)

16. S. Gunapala, et. al. Appl. Phys. Lett. **57,** 1802 (1990)

17. K. Bandara, et. al. Appl. Phys. Lett. **53,** 1931 (1988)

18. B. F. Levine, et. al. J. Appl. Phys. **76,** 6004 (1994)

19. B. Xing et. al. J. Appl. Phys. **76,** 1889 (1994)